Article

Not peer-reviewed version

Coastal Sea Ice Concentration Derived from Marine Radar Images: A Case Study from Utqiaġvik, Alaska

Félix St-Denis * , Bruno Louis Tremblay , Andrew R. Mahoney , Pacifica Askitrea Leona Mai Takata-Glushkoff

Posted Date: 6 August 2024

doi: 10.20944/preprints202408.0387.v1

Keywords: Coastal Radar; Sea Ice Concentration; Remote sensing; Utqiaġvik; Arctic

Article

Coastal Sea Ice Concentration Derived from Marine Radar Images: A Case Study from Utqiaġvik, Alaska

Félix St-Denis [1,*], L. Bruno Tremblay [1], Andrew R. Mahoney [2] and Pacifica Askitrea Leona Mai Takata-Glushkoff [2]

[1] Department of Atmospheric and Oceanic Sciences, McGill University, Montreal, Quebec, Canada; [2] Geophysical Institute, University of Alaska Fairbanks, Fairbanks, AK 99775-7320, USA; mahoney@gi.alaska.edu

* Correspondence: felix.st-denis@mail.mcgill.ca

Abstract: We apply the Canny Edge algorithm to the Utqiaġvik coastal sea ice radar system (CSIRS) to quantify open water and sea ice (landfast or drifting) concentration. The radar-derived sea ice concentration is compared against the 25-km resolution NSIDC Climate Data Record (CDR, one pixel closest to the radar field of view) and the 1-km merged MODIS-AMSR2 sea ice concentrations in the ∼11 km field of view for the year 2022-2023, when improved image contrast was first implemented. The algorithm was first optimized using sea ice concentration from 14 different images and 10 ice analysts (140 analysis in total) covering a wide range of ice condition with landfast ice, drifting ice and open water. The algorithm is also validated quantitatively against high-resolution MODIS-Terra in the visible range. Results show a correlation coefficient and mean bias error between the optimized algorithm, the CDR and MODIS-AMSR2 daily SIC of 0.18 and 0.54, and ∼ -1 and 0.9%, respectively, with an averaged inter-analyst error of ± 3%. In general, the CDR captures the melt period correctly and overestimates the SIC during the winter and freeze-up period, while the merged MODIS-AMSR2 better captures the punctual break-out events in winter including those during the freeze-up events (reduction of in SIC). Remnant issues with the detection algorithm include the false detection of sea ice in the presence, fog or precipitation (up to 20%), quantified from the summer reconstruction with known open water conditions. Coastal marine radars provide prove very useful in bridging the gap between (lower) resolution satellite-derived and in-situ (visual) sea ice conditions, and to quantify land contamination from lower resolution satellite-derived SIC.

Keywords: coastal radar; sea ice concentration; remote sensing; Utqiaġvik; Arctic

1. Introduction

In recent decades, the Arctic has witnessed significant changes in its climate with key projected impacts on permafrost, biodiversity, sea level and Inuit health [1–8]. Of all the observed changes, the most striking is the decline in the minimum sea ice extent (SIE), at a rate of -12.7 %/decade since 1979 [7,9], and the begining of the transition from a predominantly perennial to a seasonal sea ice cover since the record low SIE of 2007 [10,11]. These changes in the environment affect Arctic indigenous communities directly, in their way of living, hunting capacity, health, transportation, and infrastructures [12–15].

Output from different sensors – e.g., the Defense Meteorological Satellite Program (DMSP) Special Sensor Microwave Imager (SSM/I, 12.5-25 km) and the Special Sensor Microwave Imager/Sounder (SSMIS, 12.5-25km), the Aqua Project Advanced Microwave Scanning Radiometer 2 (AMSR2, 6.25-12.5-25km), and the Advanced Very High Resolution Radiometer (AVHRR, 2 km) – have been used since the start of the modern satellite era in the late seventies, to monitor changes in the sea ice cover – e.g., the National Snow and Ice Data Center (NSIDC) Climate Data Record (CDR) [16,17]. These sensors have spatial resolutions ranging from 1 km to 50 km [18,19] and allow for a quantitative assessment at pan-Arctic scale, including, for instance, changes in the location of the sea ice edge or detecting the presence of large polynyas [20]. Passive microwave derived sea ice concentration however suffers from land-contamination [21] and the resulting uncertainty reduces their usefulness to coastal communities. Since the mid-nineties, sea ice conditions can also be assessed from synthetic aperture radars (SARs) with spatial resolutions ranging from about 1 meters up to a kilometer (e.g., ice charts from the Canadian Ice Service, [22]). The SAR images, however, are more difficult to interpret and not consistently available on a daily basis [23–25]. Recently, high-resolution images in the visible range from MODIS were combined with sea ice information from AVHRR to produce a pan-Arctic, 1 km resolution, daily product (MODIS-AMSR2, [18]) potentially bridging the spatial scale gap between global satellite product and human scale. This dataset however is not available in real-time making not usable for operational purposes.

To address this issue, marine and coastal radars have rerently been used to monitor the stability of the landfast ice cover, sea ice drift and the presence of coastal flaw-lead polynya [26,27]. In the early 1970s, three C-band coastal radars were installed in the Sea of Okhotsk (Hokkaido, Japan), monitoring the sea ice drift over a total area of 17,500 square km^2 using cross-correlation technique [28]. More recently, new techniques emerged to derive sea ice drift estimates from radar images in both coastal and marine environment. These include dense and sparse optical flow techniques, feature tracking and phase-correlation algorithms, and normalized cross-correlation methods Mv *et al.* [29], Karvonen [30,31], Oikkonen *et al.* [32], Lund *et al.* [33]. While coastal radars have historically been used to distinguish between first-year ice, multi-year ice, and open-water [34–36], recent applications have used high-frequency radar to identify the sea ice edge and near Shirasawa *et al.* [26], and optical flow techniques to detect the landfast ice edge [29]. One of the earliest and still operating marine coastal radar is the Utqiaġvik (Alaska) Coastal Sea Ice Radar System (CSIRS) installed in 1977 to study ice deformation events (ridge building) along the coast allowing for the establishment of a stable landfast ice cover and sea ice motion of the pack ice on the northward side of the flawlead polynya [36,37]. A detailed analysis of the same radar images has also demonstrated that flickering from radar reflectors can potentially be as an early warning signal for landfast ice break-up events [37]. The latest version of the CSIRS was installed in 2007 and validated against sea ice drift estimates from a moored ice profiling sonar deployed offshore of Utqiaġvik. During its operation, the radar has detected many ice motion events near the coast, including breakout, convergence, and high-speed anomalies [38,39]. The same radar images have also supported search and rescue and marine transportation activities [39]. As of now, however, no sea ice concentration estimates have been derived directly from the CSIRS images, serving as the motivation the present article.

In this study, we derive sea ice concentration (SIC) at small scale (∼10km) and high resolution (21.5 ± 0.5 m) from the Utqiaġvik (Alaska) Coastal Sea Ice Radar System (CSIRS) [39] using image processing techniques, and compare with two existing satellite-derived products (CDR, 25 km resolution and MODIS-AMSR2, 1km). The new data product can be used to assess uncertainties and limitations in existing satellite product, including land contamination and SIC estimates in the shoulder season at freeze-up and melt onset.

The paper is organized as follows. Section 2 presents the data sets used in this study. Section 3 describes the canny sea ice edge detection algorithm and the method used to find optimal parameters. Section 4 presents the optimization steps results, and the CSIRS SIC products and its comparison to the satellite data sets. Section 5 discusses the findings and the limitations.

2. Data

2.1. (Near-Real-Time) Climate Data Record Sea Ice Concentration

We use the (Near-Real-Time) daily National Oceanic and Atmospheric Administration (NOAA) and National Snow and Ice Data Center (NSIDC) Climate Data Record of sea ice concentration version 4 (2022) and version 2 (2023), [referred to as CDR SIC in the following, 16,17]. Both datasets are a blend from the NASA Team (NT) and the NASA Bootstrap (NB) algorithms applied to Brightness Temperatures from the (NRT) Defense Meteorological Satellite Program (DMSP) Special Sensor Microwave Imager (SSM/I) and the Special Sensor Microwave Imager/Sounder (SSMIS) [17,40,41]. For each day and grid cell, the higher SIC from both algorithms is used [17]. The SICs are stored on the NSIDC polar stereographic grid with a spatial resolution of 25 km [17]. The error is 5% during winter and larger in the summer (20%, from a comparison with higher resolution products) due to difficulties in differentiating surface melt and melt ponds from open water [17,19]. In the following, we refer to the (Near-Real-Time)-CDR as the

2.2. Merged MODIS-AMSR2 Sea Ice Concentration

We use the SIC derived from Daily merged Moderated Resolution Imaging Spectroradiometer (MODIS) - Advanced Microwave Scanning Radiometer 2 (AMSR2) Thermal Infrared and Passive Microwave data available for the winter (September-May) 2022-2023 [18]. The merged dataset takes advantage of the continuous spatial coverage, but low spatial resolution (5km) of AMSR2, and high spatial resolution, but limited to cloud-free scene of MODIS [18], and resolve surface features such as leads between 60% and 90% and polynyas that are not seen by coarser Passive Microwave SIC data set [20]. To this end, the MODIS SICs are adjusted to maintain the AMSR2-derived mean SIC at 5km resolution[18]. The SIC are stored on the NSIDC polar stereographic grid with cells of a spatial resolution of 1 km [18]. The error on the merged product are between 5% and 10% from February to April and up to 18% in May [18], when the MODIS errors are larger (30%).

2.3. Coastal Sea Ice Radar System Images

We use 4-minute snapshots from the University of Alaska Fairbanks coastal sea ice radar in Utqiaġvik available in near-real time at https://seaice.alaska.edu/gi/observatories/barrow_radar/ [36–39,42]. The radar is located 22.5 m above sea level on the rooftop of local bank downtown Utqiaġvik [39]. The operating radar is a 25 kW Furuno FAR2117X band system with a 2.44 open array antenna [39]. The radar can detect sea ice features up to 11 km depending on atmospheric conditions in its current configuration [39]. Specifically, fog and precipitation attenuate the radar signals, which makes the identification of sea ice features more difficult [29]. The images are reprojected to a Cartesian plane where each pixel is 21.5 ± 5 m [38]. We note that coastal sea ice radars are mostly sensitive to ridges and floe edges – due to the small grazing angle–, with little energy reflected from smooth surface inside the pack of ice [38].

3. Methods

3.1. Floe Edge Detection Algorithms

We take advantage of the radar sensitivity to floe edges to identify ice floes and open water using the canny edge detection operator [43,44] and the contour detection algorithm [45] from the open-source computer vision library OpenCV.

The canny edge and Suzuki algorithms extract floe edges from the masked gray-scale images in six separate steps [43,45]. First, the land, Elson lagoon and the boundary at the edge of the field of view are masked from all frames to limit the analysis to the ocean field of view that is resolved by the radar (Figure 1 a-b). Second, a 5x5 Gaussian filter is applied to remove noise, followed by a two-dimensional 3x3 Sobel kernel operator to identify edge gradients. Third, the edge gradients are refined using a non-maximum suppression step keeping only the local maximum in gradients. Fourth, the floe edges are formed by applying a two-threshold hysteresis procedure where pixels with a gradient larger than an upper threshold (T_{up}) are considered as an edge, and pixels with a gradient in between the lower and upper thresholds ($T_{low} <$ gradient $< T_{up}$) are considered as an edge only if they are connected to another edge pixel [43,46]. A threshold below the lower threshold is always rejected. Fifth, a binary mask is used to remove the radar image boundary where large gradients are present. Sixth, the Suzuki algorithm is used to link the points identified as edges by the canny edge algorithm [45]. Specifically, the edges are dilated by convoluting the image with a square kernel and with the pixel below the anchor point equal to the maximum value within the kernel square, resulting in well-defined (sharp gradient) edge segments that are all connected together [46, Figure 1 d]. The optimization procedure to determine the upper and lower thresholds and kernels is discussed below in subsection 3.3.

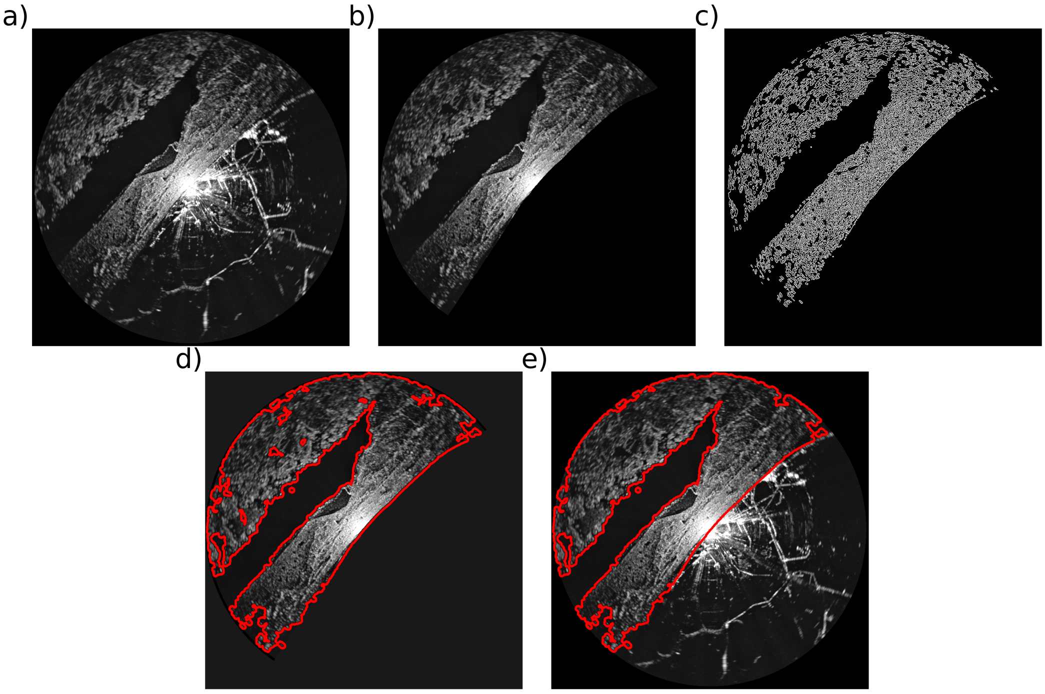

Figure 1. Images from March 11, 2022, taken after each algorithm steps: a) initial image, b) masked out image, c) the output of the Canny edge algorithm, d) the contours found from the edges and e) the final sea ice contour.

3.2. Post-Processing

We first delete (rare events of) closed contours within larger contours, assuming that they are primarily shadows behind ridges, rather than open water. This is confirmed visually from inspection of the animated radar images for 10 scenes also analyzed by human analysts (see section 3.3 for details) where detection of ice and open water is easier. In turn, the areas of low-radar return – in the shadow of ridges or covered by smooth ice inside edges – are marked as sea ice despite having a similar signature as open water [38, Figure 1 e]. Finally, we calculate the (sea ice) area within each closed contours. The sea ice concentration is the ratio of the sea ice area to the total radar ocean field of view.

3.3. Parameters Optimization

Following [47], we use the sea ice edge analysis of fourteen frames by 10 different analysts from our research group as truth for the optimization of the two thresholds and kernel. The fourteen frames, selected in the 2022-2023 winter season, are representative of the full range of sea ice conditions seen by the radar, i.e., 100% sea ice, 100% open water, and a mixture of open-water, landfast, and drifting ice.

The floe detection algorithm was run over the full parameter space for the lower and upper thresholds 8-bits (0 – 255) and kernel dilation window size, (3, 5, 7, 9, 11, 13) to find the set of parameters that minimizes the root mean square error (RMSE) and slope of the best line fit of sea ice concentration for 14 different frames produced by the algorithm from 10 analysts. We choose the RMSE for the loss function instead of the mean bias error (MBE) because we want an algorithm that performs well for a wide range of SIC.

3.4. CSIRS Daily SIC Product

The CSIRS daily mean SIC is calculated from the output of the floe detection algorithm run with optimal parameters on each 4 min frame (360 in total) for each day of 2022-2023. Missing frames are omitted from the calculation.

3.5. Comparison of SIC Products

We perform a qualitative comparison of the NASA WorldView MODIS Terra (https://worldview.earthdata.nasa.gov) and the marine radar images, and a point-by point comparison between the merged MODIS-AMSR2 and an interpolated coarse-grained CSIRS SIC of similar spatial resolution (1 km), for April 14, 2022, a day when no clouds were present. We give an estimate of the spread in the merged MODIS-ASMR2 from the mean, minimum and maximum SIC for all grid cells that are within the field of view of the radar for comparison with the reconstructed sea ice concentration from the marine radar (Figure 2). For the CDR dataset, only one grid cell is in the field of view of the marine radar and no spread estimate is possible. We use the standard deviation as a proxy for the error (associated with poor radar return and land contamination in both datasets. For the correlation between CDR, MODIS-AMSR2 and CSIRS dataset, the anomaly time series are calculated by removing a 30-day running mean.

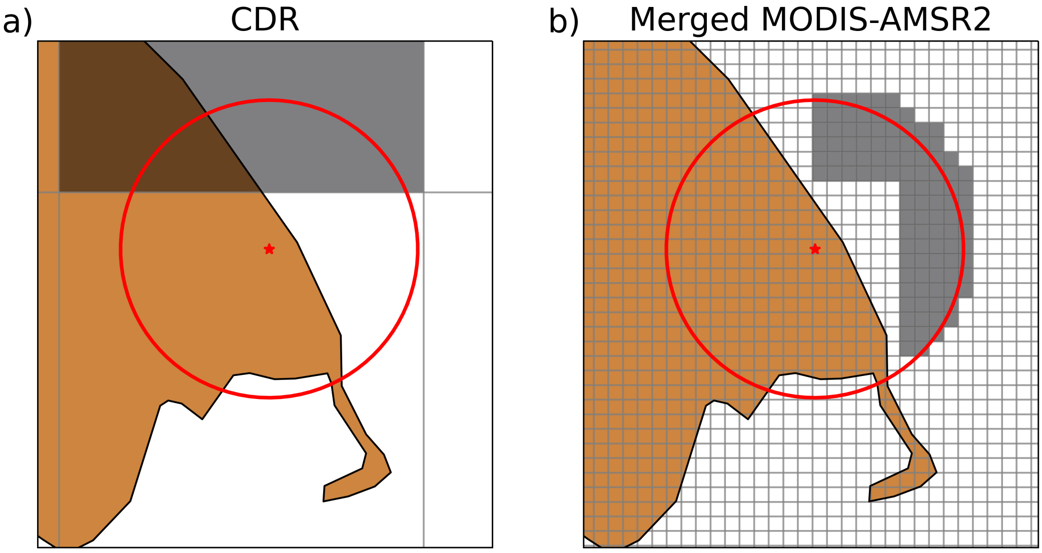

Figure 2. CDR (a) and merged MODIS-AMSR2 (b) grid cells used for the comparison with the marine radar. Utqiagvik and the radar range are marked with a red star and circle.

4. Results

4.1. Optimization/Validation

The best line fit between the canny edge algorithm and the analysis of 14 images from 10 analysts is obtained with the 11x11 kernel, and thresholds in pixel intensity (T_{low} and T_{high}) equal to 4 and 82, respectively (Figure 3 (a)). The resulting slope and intercept of the linear regression are 0.94 and 0.036, respectively, while the RMSE is 0.035. An optimization based on the RMSE instead results in a small reduction in error (RMSE = 0.035) but a large maximum bias (= 0.1 for SIC=1) and is therefore not the preferred option (Figure 3 (a)). (Figure 3 (b)). The inter-analyst error (= 0.026) – a measure of the error on the "truth" – is small compared with the RMSE indicating that most of the difference between the kernels can be attributed to the algorithm (Figure 3 b). Finally, the algorithm can incorrectly identify open water as sea ice when there is fog or noise in the image, which can explain the radar SIC's overestimation compared to the analyst's.

doi:10.20944/preprints202408.0387.v1

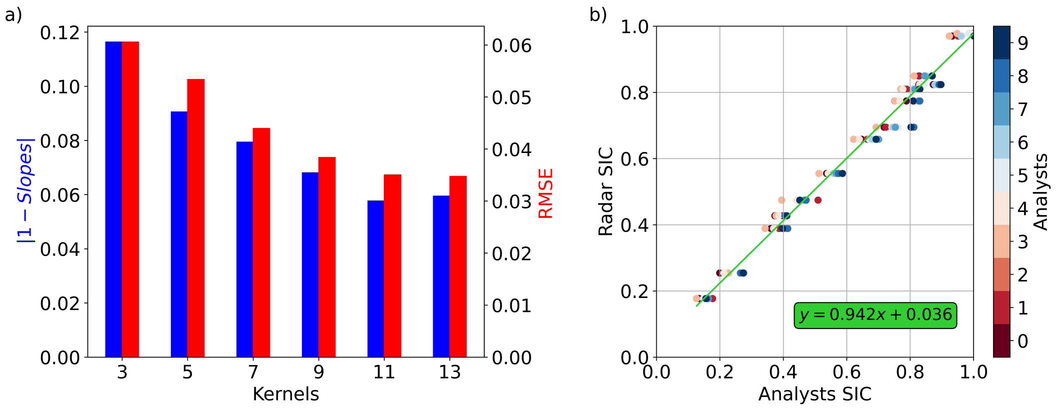

Figure 3. (a) Departure of the best 1:1 line fit (blue) and RMSE (red) for each kernels. (b) Scatter plot of SIC derived from the radar images with the optimal set of parameters and SIC from the 10 analysts (colorbar), including the best-line fit (green line). Each of the horizontal lines represent a different image. The inter-analyst averaged error is 0.026.

The detection algorithm with the optimal parameter successfully identifies most of the sea ice edge features observed by MODIS Terra on April 14, 2022, under cloud-free conditions (Figure 4 (a-b)). The open water and the narrow band of open water south-west and directly in front of the building on which the CSIRS is mounted, where the CSIRS is located, are well seen. However, the open water to the north and the water between the broken floes to the north of the radar image however are missed by the algorithm. (Figure 4 (a-b)). Additionally, the rugged features of the sea ice edge are consistently present in both images. The coarse-grain CSIRS SIC estimate also correlates well with the daily merged MODIS-AMSR2 SIC, with the correlation coefficient exceeding 0.6 for most of the day. The drop in correlation during the middle of the day is presumably due to the swaths composing the merged MODIS-AMSR2 SIC were not taken at this time. Overall, the detection algorithm can identify most sea ice edges present in the MODIS image, considering that the exact acquisition time of the merged MODIS-AMSR2 SIC passing over the marine radar field of view is not known.

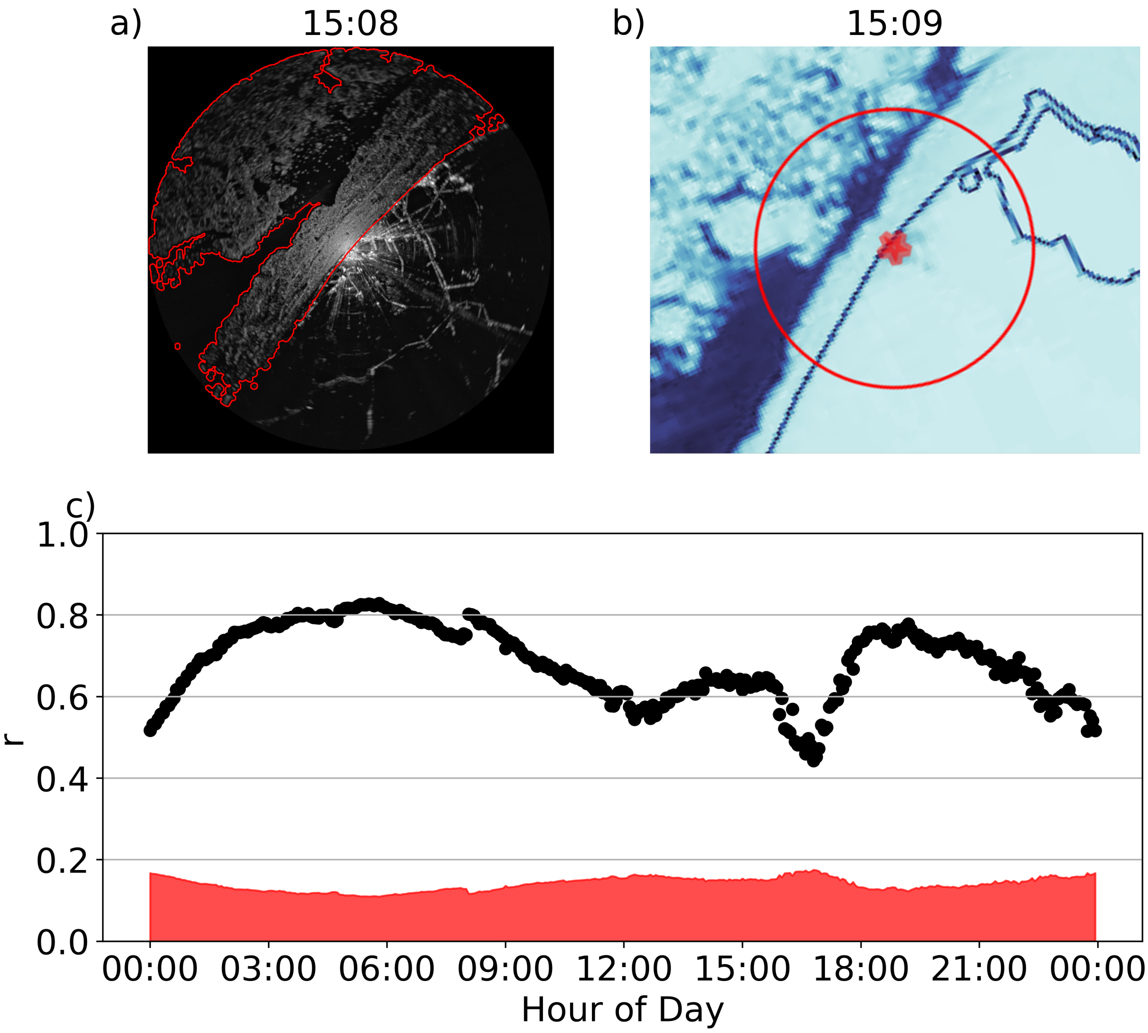

Figure 4. (a) Synchronous Marine radar image including sea ice edge (red) from the detection algorithm and (b) MODIS Terra image at 15:08 and 15:09 local time (AKDT), respectively. Time series of Pearson correlation coefficient (*r*) between all 4-min images (360 in total) coarse-grained (1 km) CSIRS SIC and the merged MODIS-AMSR2 SIC (c) for April 14, 2022. The red shading correspond to the 95% confidence interval.

4.2. CSIRS Reconstructed Sea Ice Concentration

4.2.1. Daily SIC

The CDR data and the merged MODIS-AMSR2 overestimate SIC with respect to the CSIRS with an MBE equal to -0.10 and $-9.0 \cdot 10^{-3}$, respectively (Figure 5 a, Table 1). The correlation coefficients between the daily CDR, MODIS-AMSR2 and the reconstructed SIC from CSIRS are low (r=0.18) and moderate (r=0.54), both significant at the 95% level, and RMSE errors of 0.34 and 0.29, respectively (Table 1). At weekly and monthly time scale, the correlation coefficients for the CDR and MODIS-AMSR2 increase to 0.276-0.71 and 0.68-0.59, respectively (results not shown). In winter, the CDR generally underestimates short-lived low SIC (breakout) events – most notably in early winter 2023 (Jan-Feb 2023) – while MODIS-AMSR2 SICs are in general agreement with observed values (Figure 5 a). In the break-up period (Jun-Jul 2022), CDR is in general agreement with observations, while during the freeze-up (Dec 2022 - Jan 2023) both satellite leads the observed ice onset by approximately 10 days, perhaps due to land contamination with an earlier onset of snow presence on land [48]. In the summer, the algorithm incorrectly identifies clouds as sea ice with reconstructed SICs ranging between 20-25%. The CDR SIC on the other hand correctly identified open water during this period (Fig 4-5).

Table 1. Pearson correlation coefficient (*r*), root mean square error (RMSE) and mean bias error (MBE) for the daily, 7-day and 31-day running mean CSIRS SIC, CDR and merged MODIS-AMSR2 SIC for 2022 and 2023.

	SIC Type	*r*	RMSE	MBE
CDR	Daily	0.18	0.34	-0.010
	7 Days RM	0.26	0.31	-0.010
	31 Days RM	0.71	0.28	-0.010
merged MODIS-AMSR2	Daily	0.54	0.29	$-9.0 \cdot 10^{-3}$
	7 Days RM	0.68	0.23	$-8.9 \cdot 10^{-3}$
	31 Days RM	0.59	0.20	$8.0 \cdot 10^{-3}$

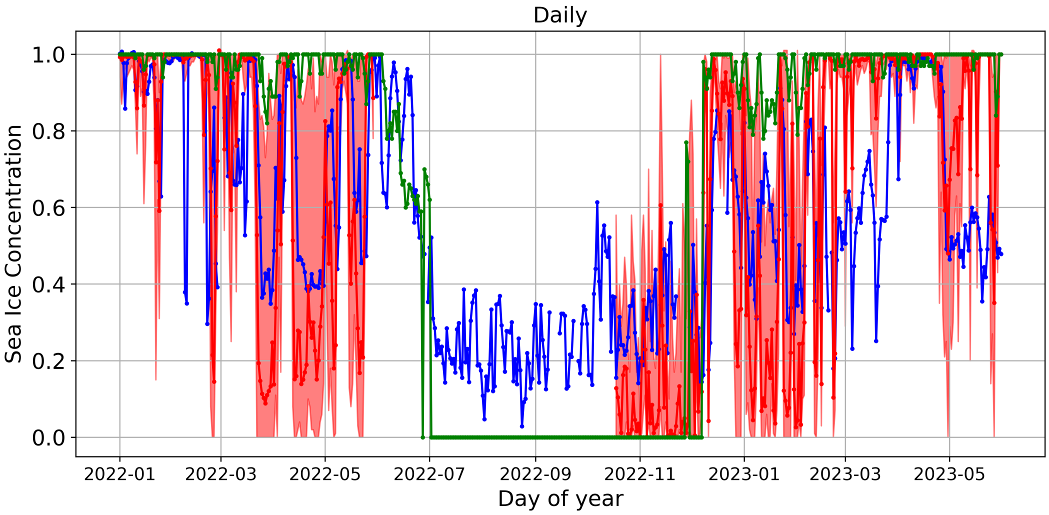

Figure 5. Daily time series of the SIC derived from the radar (blue), the CDR (green), and the merged MODIS-AMSR2 (red) for 2022 to 2023 in function of the Julian days starting January 1st, 2022. The shading around the MODIS-AMSR2 and CDR represents the spread of the SIC. The holes in the time series represent the non-availability of the data.

5. Discussion and Conclusions

To first order, both the CDR and the merged MODIS-AMSR2 datasets captures the same seasonality of SIC at Utqiagvik as the CSIRS. In mid- to late-winter, spring and early summer, the CDR SIC is in good agreement with the CSIRS SIC, while the merged MODIS-AMSR2 is in better agreement in the fall freeze-up and early winter. In early winter of 2023, the CDR underestimates break-up events while the MODIS-AMSR2 under-estimates the CSIRS SIC in mid- to late-winter, presumably due to the AMSR2 mask not capturing the landfast ice area near the coast (see Figure 2). In the summer, the canny edge algorithm interpret the presence of fog and clouds as sea ice near the coast leading to a positive bias in the reconstruction.

In summary, the floe edge detection algorithm is successful at identifying sea ice and open water, including break-up events under all conditions, but misinterpret fog and cloud as sea ice particularly in the summer [37,49,50]. Marine radar images along with floe detection algorithm can be use jointly to assess uncertainties associated with land contamination in low and high resolution satellite products. Raising the coastal radar height above ground (if at all possible) and therefore radar range would provide a useful data set to evaluate changes in land contamination with distance from the coast and would reduce shadow effect from nearby ridges. Two new marine radars were installed recently in Nome and Gambell (AK). Future work include testing the proposed algorithm on the new radar images from locations with very different sea ice regimes as well as implementing an edge tracking feature in time to even better estimate the sea ice concentration.

Author Contributions: Conceptualization, B.T, F.S and P. T. ; methodology, B.T and F.S.; software, F.S.; validation, B.T. and F.S.; formal analysis, F.S., B.T. and A.M.; investigation, B.T. and F.S.; resources, F.S. and B.T.; data curation, F.S. and A.M.; writing—original draft preparation, F. S.; writing—review and editing, B.T. and A.M.; visualization, F.S.; supervision, B.T.; project administration, B.T.; funding acquisition, B.T. and A.M. All authors have read and agreed to the published version of the manuscript.

Funding: This project is a contribution to the ArcNAV project entitled: Arctic Robust Communities-Navigating Adaptation to Variability funded by the National Science Foundation – Office of Polar Program (project 1928126, 1928259) awarded to Tremblay and Mahoney, and a Discovery grant from the Natural Sciences and Engineering Research Council, awarded to Tremblay. This work also benefited from academic and financial support of McGill University and Québec–Océan.

Data Availability Statement: The original contributions presented in the study are included in the article/supplementary material, further inquiries can be directed to the corresponding author/s. The CSIRS images and the CDR Sea Ice Concentration dataset are publicly available at https://seaice.alaska.edu/gi/observatories/barrow_radar/ and https://nsidc.org/data/g02202/versions/4#anchor-documentation, respectively. The code produced for this study can be made publicly available if asked.

Acknowledgments: Félix St-Denis is thankful to the Institute of Environmental Physics, University of Bremen, for the provision of the merged MODIS-AMSR2 sea-ice concentration data at https://data.seaice.uni-bremen.de/modis_amsr2 (last access 2024-06-20). Félix St-Denis is grateful to the Fond de Recherche du Québec Nature et Technologie (FRQNT), the Natural Sciences and Engineering Research Council of Canada (NSERC) and the North Slope Borough of Alaska (Eben Hopson Fellowship) for scholarships received during the course of this work. Félix St-Denis and Bruno Tremblay thank Joshua Jones for the insightful comments about the work presented in this paper and Samuel George for the frontline work with the CSIRS.

Conflicts of Interest: The authors declare no conflict of interest.

References

1. Stroeve, J.C.; Markus, T.; Boisvert, L.; Miller, J.; Barrett, A. Changes in Arctic melt season and implications for sea ice loss. *Geophysical Research Letters* **2014**, *41*, 1216–1225. _eprint: https://onlinelibrary.wiley.com/doi/pdf/10.1002/2013 doi:10.1002/2013GL058951.
2. Ford, J.D.; Willox, A.C.; Chatwood, S.; Furgal, C.; Harper, S.; Mauro, I.; Pearce, T. Adapting to the Effects of Climate Change on Inuit Health. *American Journal of Public Health* **2014**, *104*, e9–e17. doi:10.2105/AJPH.2013.301724.
3. Post, E.; Alley, R.B.; Christensen, T.R.; Macias-Fauria, M.; Forbes, B.C.; Gooseff, M.N.; Iler, A.; Kerby, J.T.; Laidre, K.L.; Mann, M.E.; Olofsson, J.; Stroeve, J.C.; Ulmer, F.; Virginia, R.A.; Wang, M. The polar regions in a 2°C warmer world. *Science Advances* **2019**, *5*, eaaw9883. doi:10.1126/sciadv.aaw9883.
4. Box, J.E.; Colgan, W.T.; Christensen, T.R.; Schmidt, N.M.; Lund, M.; Parmentier, F.J.W.; Brown, R.; Bhatt, U.S.; Euskirchen, E.S.; Romanovsky, V.E.; Walsh, J.E.; Overland, J.E.; Wang, M.; Corell, R.W.; Meier, W.N.; Wouters, B.; Mernild, S.; Mård, J.; Pawlak, J.; Olsen, M.S. Key indicators of Arctic climate change: 1971–2017. *Environmental Research Letters* **2019**, *14*, 045010. doi:10.1088/1748-9326/aafc1b.
5. Middleton, J.; Cunsolo, A.; Jones-Bitton, A.; Wright, C.J.; Harper, S.L. Indigenous mental health in a changing climate: a systematic scoping review of the global literature. *Environmental Research Letters* **2020**, *15*, 053001. doi:10.1088/1748-9326/ab68a9.
6. Middleton, J.; Cunsolo, A.; Jones-Bitton, A.; Shiwak, I.; Wood, M.; Pollock, N.; Flowers, C.; Harper, S.L. “We’re people of the snow:” Weather, climate change, and Inuit mental wellness. *Social Science & Medicine* **2020**, *262*, 113137. doi:10.1016/j.socscimed.2020.113137.
7. Meier, W.; Stroeve, J. An Updated Assessment of the Changing Arctic Sea Ice Cover. *Oceanography* **2022**. doi:10.5670/oceanog.2022.114.
8. Schuur, E.A.; Abbott, B.W.; Commane, R.; Ernakovich, J.; Euskirchen, E.; Hugelius, G.; Grosse, G.; Jones, M.; Koven, C.; Leshyk, V.; Lawrence, D.; Loranty, M.M.; Mauritz, M.; Olefeldt, D.; Natali, S.; Rodenhizer, H.; Salmon, V.; Schädel, C.; Strauss, J.; Treat, C.; Turetsky, M. Permafrost and Climate Change: Carbon

Cycle Feedbacks From the Warming Arctic. *Annual Review of Environment and Resources* **2022**, *47*, 343–371. doi:10.1146/annurev-environ-012220-011847.

9. Stroeve, J.; Notz, D. Changing state of Arctic sea ice across all seasons. *Environmental Research Letters* **2018**, *13*, 103001. Publisher: IOP Publishing, doi:10.1088/1748-9326/aade56.
10. Nghiem, S.V.; Rigor, I.G.; Perovich, D.K.; Clemente-Colón, P.; Weatherly, J.W.; Neumann, G. Rapid reduction of Arctic perennial sea ice. *Geophysical Research Letters* **2007**, *34*. _eprint: https://onlinelibrary.wiley.com/doi/pdf/10.1029/2007 doi:10.1029/2007GL031138.
11. Comiso, J.C. Large Decadal Decline of the Arctic Multiyear Ice Cover. *Journal of Climate* **2012**, *25*, 1176–1193. Publisher: American Meteorological Society Section: Journal of Climate, doi:10.1175/JCLI-D-11-00113.1.
12. Ford, J.D.; Pearce, T.; Canosa, I.V.; Harper, S. The rapidly changing Arctic and its societal implications. *WIREs Climate Change* **2021**, *12*, e735. _eprint: https://onlinelibrary.wiley.com/doi/pdf/10.1002/wcc.735, doi:10.1002/wcc.735.
13. Hauser, D.D.W.; Whiting, A.V.; Mahoney, A.R.; Goodwin, J.; Harris, C.; Schaeffer, R.J.; Schaeffer, R.; Laxague, N.J.M.; Subramaniam, A.; Witte, C.R.; Betcher, S.; Lindsay, J.M.; Zappa, C.J. Co-production of knowledge reveals loss of Indigenous hunting opportunities in the face of accelerating Arctic climate change. *Environmental Research Letters* **2021**, *16*, 095003. doi:10.1088/1748-9326/ac1a36.
14. Ford, J.D. Dangerous climate change and the importance of adaptation for the Arctic's Inuit population. *Environmental Research Letters* **2009**, *4*, 024006. doi:10.1088/1748-9326/4/2/024006.
15. Ford, J.D.; Clark, D.; Pearce, T.; Berrang-Ford, L.; Copland, L.; Dawson, J.; New, M.; Harper, S.L. Changing access to ice, land and water in Arctic communities. *Nature Climate Change* **2019**, *9*, 335–339. Number: 4 Publisher: Nature Publishing Group, doi:10.1038/s41558-019-0435-7.
16. Meier, W.; Fetterer, F.; Windnagel, A.; Stewart, S. Near-Real-Time NOAA/NSIDC Climate Data Record of Passive Microwave Sea Ice Concentration, Version 2, 2021. doi:10.7265/TGAM-YV28.
17. Meier, W.; Fetterer, F.; Windnagel, A.; Stewart, S. NOAA/NSIDC Climate Data Record of Passive Microwave Sea Ice Concentration, Version 4, 2021. doi:10.7265/EFMZ-2T65.
18. Ludwig, V.; Spreen, G.; Pedersen, L.T. Evaluation of a New Merged Sea-Ice Concentration Dataset at 1 km Resolution from Thermal Infrared and Passive Microwave Satellite Data in the Arctic. *Remote Sensing* **2020**, *12*, 3183. Number: 19 Publisher: Multidisciplinary Digital Publishing Institute, doi:10.3390/rs12193183.
19. Kern, S.; Lavergne, T.; Notz, D.; Pedersen, L.T.; Tonboe, R. Satellite passive microwave sea-ice concentration data set inter-comparison for Arctic summer conditions. *The Cryosphere* **2020**, *14*, 2469–2493. doi:10.5194/tc-14-2469-2020.
20. Ludwig, V.; Spreen, G.; Haas, C.; Istomina, L.; Kauker, F.; Murashkin, D. The 2018 North Greenland polynya observed by a newly introduced merged optical and passive microwave sea-ice concentration dataset. *The Cryosphere* **2019**, *13*, 2051–2073. doi:10.5194/tc-13-2051-2019.
21. Parkinson, C.L.; Cavalieri, D.J. Arctic sea ice 1973–1987: Seasonal, regional, and interannual variability. *Journal of Geophysical Research: Oceans* **1989**, *94*, 14499–14523. _eprint: https://onlinelibrary.wiley.com/doi/pdf/10.1029/JC094iC10 doi:10.1029/JC094iC10p14499.
22. Canadian Ice Service. Canadian Ice Service Arctic Regional Sea Ice Charts in SIGRID-3 Format, Version 1 **2009**. Publisher: NSIDC, doi:10.7265/N51V5BW9.
23. Dierking, W. Sea Ice Monitoring by Synthetic Aperture Radar. *Oceanography* **2013**, *26*, 100–111. Publisher: Oceanography Society.
24. Soh, L.K.; Tsatsoulis, C. Texture analysis of SAR sea ice imagery using gray level co-occurrence matrices. *IEEE Transactions on Geoscience and Remote Sensing* **1999**, *37*, 780–795. Conference Name: IEEE Transactions on Geoscience and Remote Sensing, doi:10.1109/36.752194.
25. Ochilov, S.; Clausi, D.A. Operational SAR Sea-Ice Image Classification. *IEEE Transactions on Geoscience and Remote Sensing* **2012**, *50*, 4397–4408. Conference Name: IEEE Transactions on Geoscience and Remote Sensing, doi:10.1109/TGRS.2012.2192278.
26. Shirasawa, K.; Ebuchi, N.; Leppäranta, M.; Takatsuka, T. Ice-edge detection from Japanese C-band radar and high-frequency radar coastal stations. *Annals of Glaciology* **2013**, *54*, 59–64. Publisher: Cambridge University Press, doi:10.3189/2013AoG62A007.
27. Nicolaus, M.; Perovich, D.K.; Spreen, G.; Granskog, M.A.; von Albedyll, L.; Angelopoulos, M.; Anhaus, P.; Arndt, S.; Belter, H.J.; Bessonov, V.; Birnbaum, G.; Brauchle, J.; Calmer, R.; Cardellach, E.; Cheng, B.; Clemens-Sewall, D.; Dadic, R.; Damm, E.; de Boer, G.; Demir, O.; Dethloff, K.; Divine, D.V.; Fong, A.A.;

Fons, S.; Frey, M.M.; Fuchs, N.; Gabarró, C.; Gerland, S.; Goessling, H.F.; Gradinger, R.; Haapala, J.; Haas, C.; Hamilton, J.; Hannula, H.R.; Hendricks, S.; Herber, A.; Heuzé, C.; Hoppmann, M.; Høyland, K.V.; Huntemann, M.; Hutchings, J.K.; Hwang, B.; Itkin, P.; Jacobi, H.W.; Jaggi, M.; Jutila, A.; Kaleschke, L.; Katlein, C.; Kolabutin, N.; Krampe, D.; Kristensen, S.S.; Krumpen, T.; Kurtz, N.; Lampert, A.; Lange, B.A.; Lei, R.; Light, B.; Linhardt, F.; Liston, G.E.; Loose, B.; Macfarlane, A.R.; Mahmud, M.; Matero, I.O.; Maus, S.; Morgenstern, A.; Naderpour, R.; Nandan, V.; Niubom, A.; Oggier, M.; Oppelt, N.; Pätzold, F.; Perron, C.; Petrovsky, T.; Pirazzini, R.; Polashenski, C.; Rabe, B.; Raphael, I.A.; Regnery, J.; Rex, M.; Ricker, R.; Riemann-Campe, K.; Rinke, A.; Rohde, J.; Salganik, E.; Scharien, R.K.; Schiller, M.; Schneebeli, M.; Semmling, M.; Shimanchuk, E.; Shupe, M.D.; Smith, M.M.; Smolyanitsky, V.; Sokolov, V.; Stanton, T.; Stroeve, J.; Thielke, L.; Timofeeva, A.; Tonboe, R.T.; Tavri, A.; Tsamados, M.; Wagner, D.N.; Watkins, D.; Webster, M.; Wendisch, M. Overview of the MOSAiC expedition: Snow and sea ice. *Elementa: Science of the Anthropocene* **2022**, *10*, 000046. doi:10.1525/elementa.2021.000046.

28. Tabata, T. Sea-ice Reconnaissance by Radar. *Journal of Glaciology* **1975**, *15*, 215–224. Publisher: Cambridge University Press, doi:10.3189/S0022143000034389.
29. Mv, R.; Jones, J.; Eicken, H.; Kambhamettu, C. Extracting Quantitative Information on Coastal Ice Dynamics and Ice Hazard Events From Marine Radar Digital Imagery. *IEEE Transactions on Geoscience and Remote Sensing* **2013**, *51*, 2556–2570. doi:10.1109/TGRS.2012.2217972.
30. Karvonen, J. Tracking the motion of recognizable sea-ice objects from coastal radar image sequences. *Annals of Glaciology* **2013**, *54*, 41–49. Publisher: Cambridge University Press, doi:10.3189/2013AoG62A042.
31. Karvonen, J. Virtual radar ice buoys – a method for measuring fine-scale sea ice drift. *The Cryosphere* **2016**, *10*, 29–42. doi:10.5194/tc-10-29-2016.
32. Oikkonen, A.; Haapala, J.; Lensu, M.; Karvonen, J. Sea ice drift and deformation in the coastal boundary zone. *Geophysical Research Letters* **2016**, *43*, 10,303–10,310. _eprint: https://onlinelibrary.wiley.com/doi/pdf/10.1002/2016GL06 doi:10.1002/2016GL069632.
33. Lund, B.; Graber, H.C.; Persson, P.O.G.; Smith, M.; Doble, M.; Thomson, J.; Wadhams, P. Arctic Sea Ice Drift Measured by Shipboard Marine Radar. *Journal of Geophysical Research: Oceans* **2018**, *123*, 4298–4321. _eprint: https://onlinelibrary.wiley.com/doi/pdf/10.1029/2018JC013769, doi:10.1029/2018JC013769.
34. Flock, W.L. Monitoring Open Water and Sea Ice in the Bering Strait by Radar. *IEEE Transactions on Geoscience Electronics* **1977**, *15*, 196–202. Conference Name: IEEE Transactions on Geoscience Electronics, doi:10.1109/TGE.1977.294492.
35. Haykin, S.; Currie, B.; Lewis, E.; Nickerson, K. Surface-based radar imaging of sea ice. *Proceedings of the IEEE* **1985**, *73*, 233–251. Conference Name: Proceedings of the IEEE, doi:10.1109/PROC.1985.13136.
36. Shapiro, L.H.; Metzner, R.C. Nearshore iceconditions from radar data, Point Barrow, Alaska. *Fairbanks: University of Alaska Fairbanks* **1989**.
37. Mahoney, A.; Eicken, H.; Shapiro, L. How fast is landfast sea ice? A study of the attachment and detachment of nearshore ice at Barrow, Alaska. *Cold Regions Science and Technology* **2007**, *47*, 233–255. doi:10.1016/j.coldregions.2006.09.005.
38. Mahoney, A.R.; Eicken, H.; Fukamachi, Y.; Ohshima, K.I.; Simizu, D.; Kambhamettu, C.; Rohith, M.; Hendricks, S.; Jones, J. Taking a look at both sides of the ice: comparison of ice thickness and drift speed as observed from moored, airborne and shore-based instruments near Barrow, Alaska. *Annals of Glaciology* **2015**, *56*, 363–372. doi:10.3189/2015AoG69A565.
39. Kettle, N.P.; Abdel-Fattah, D.; Mahoney, A.R.; Eicken, H.; Brigham, L.W.; Jones, J. Linking Arctic system science research to decision maker needs: co-producing sea ice decision support tools in Utqiaġvik, Alaska. *Polar Geography* **2020**, *43*, 206–222. doi:10.1080/1088937X.2019.1707318.
40. Cavalieri, D.J.; Gloersen, P.; Campbell, W.J. Determination of sea ice parameters with the NIMBUS 7 SMMR. *Journal of Geophysical Research: Atmospheres* **1984**, *89*, 5355–5369. doi:10.1029/JD089iD04p05355.
41. Comiso, J.C. Characteristics of Arctic winter sea ice from satellite multispectral microwave observations. *Journal of Geophysical Research* **1986**, *91*, 975. doi:10.1029/JC091iC01p00975.
42. Druckenmiller, M.L.; Eicken, H.; Johnson, M.A.; Pringle, D.J.; Williams, C.C. Toward an integrated coastal sea-ice observatory: System components and a case study at Barrow, Alaska. *Cold Regions Science and Technology* **2009**, *56*, 61–72. doi:10.1016/j.coldregions.2008.12.003.

doi:10.20944/preprints202408.0387.v1

43. Canny, J. A Computational Approach to Edge Detection. *IEEE Transactions on Pattern Analysis and Machine Intelligence* **1986**, *PAMI-8*, 679–698. Conference Name: IEEE Transactions on Pattern Analysis and Machine Intelligence, doi:10.1109/TPAMI.1986.4767851.
44. Bradski, G. The OpenCV Library. *Dr. Dobb's Journal of Software Tools* **2000**.
45. Suzuki, S.; be, K. Topological structural analysis of digitized binary images by border following. *Computer Vision, Graphics, and Image Processing* **1985**, *30*, 32–46. doi:10.1016/0734-189X(85)90016-7.
46. Bradski, G.R.; Kaehler, A. *Learning OpenCV: computer vision with the OpenCV library*, 1. ed., [nachdr.] ed.; Software that sees, O'Reilly: Beijing, 2011.
47. Cheng, A.; Casati, B.; Tivy, A.; Zagon, T.; Lemieux, J.F.; Tremblay, L.B. Accuracy and inter-analyst agreement of visually estimated sea ice concentrations in Canadian Ice Service ice charts using single-polarization RADARSAT-2. *The Cryosphere* **2020**, *14*, 1289–1310. Publisher: Copernicus GmbH, doi:10.5194/tc-14-1289-2020.
48. Parkinson, C.L. Spatial patterns of increases and decreases in the length of the sea ice season in the north polar region, 1979–1986. *Journal of Geophysical Research: Oceans* **1992**, *97*, 14377–14388. _eprint: https://onlinelibrary.wiley.com/doi/pdf/10.1029/92JC01367, doi:10.1029/92JC01367.
49. Jones, J.; Eicken, H.; Mahoney, A.; Mv, R.; Kambhamettu, C.; Fukamachi, Y.; Ohshima, K.I.; George, J.C. Landfast sea ice breakouts: Stabilizing ice features, oceanic and atmospheric forcing at Barrow, Alaska. *Continental Shelf Research* **2016**, *126*, 50–63. doi:10.1016/j.csr.2016.07.015.
50. Aucoin, S.; Tremblay, B.; Newton, R. Coastal Sea-Ice Break-Up Events in Beringia. *McGill Science Undergraduate Research Journal* **2022**, *17*, 18–22. Number: 1, doi:10.26443/msurj.v17i1.172.